Supporting Information

Boosted Urea Electrooxidation Activity by Dynamic Steady Blending CoOOH-Ni(OH)₂ Nanoclusters for H₂ Production in a pH-asymmetric Electrolyzer

Shih-Mao Peng,[1,2][#] Shu-Ting Chang,[2][#] Chia-Che Chang,[3][#] Priyadarshini HN,[2] Chun-Chih Chang,[4]* Kuan-Chang Wu,[2] Yung-Hung Huang,[5] Yi-Chia Chen,[5] Tsung-Rong Kuo,[6] Chih-Wen Pao,[3] Jeng-Lung Chen,[3] Di-Yan Wang[5]*

[1] Graduate Institute of Biomedical Materials & Tissue Engineering, Taipei Medical University, Taipei 11031, Taiwan

[2] Department of Chemistry, Tunghai University, Taichung 40704, Taiwan

[3] National Synchrotron Radiation Research Center (NSRRC), Hsinchu 30076, Taiwan

[4] Department of Chemical and Materials Engineering, Chinese Culture University, Taipei 11114, Taiwan

[5] Department of Chemistry, National Taiwan Normal University, Taipei, 11677, Taiwan

[6] Graduate Institute of Nanomedicine and Medical Engineering, College of Biomedical Engineering, Taipei Medical University, Taipei 11031, Taiwan

[#]Shih-Mao Peng, Shu-Ting Chang and Chia-Che Chang contributed equally to this work.

Corresponding author: zjz8@ulive.pccu.edu.tw (C.-C Chang) and diyanwang@ntnu.edu.tw (D.-Y Wang).

Thermodynamic Treatment. The Gibbs free energy (G) for the energy difference (ΔG) between any adsorbate pair on the CoNiO$_{x\ (x=2\sim3)}$ (100) surface was defined as $\Delta G = \Delta H - T\Delta S$, in which ΔH is enthalpy change and ΔS is entropy change of the system. ΔH was estimated as $\Delta(E + ZPE + U_{vib})$ with E representing the average electronic energy of DFT, ZPE representing zero-point energy correction, and E_{vib} representing the internal energy correction of vibrational models (the relative translational and rotational contribution for any adsorbate

pair was assumed cancelled out).[1] ΔS was predicted by the vibrational partition function using harmonic vibrations. Furthermore, the zero-point energies (ZPE) and entropy contributions to free energies at room temperature (298.15 K).

The potential calculation in asymmetric electrocatalysis system

The theory potential of water splitting in asymmetric electrocatalysis system according to Nernst equation:

In cathodic reaction: $2H^+ + 2e^- \rightarrow H_{2(g)}$

$$E_{\frac{H^+}{H_2}} = E_{\frac{H^+}{H_2}}^{\theta} + \frac{RT}{4F}\ln\frac{[\alpha_{H^+}]^2}{[\alpha_{H_2}]} = 0\ V - 0.0591 \times pH_{Anode} = 0\ V\ (pH = 0)$$

Anodic reaction: $4OH^- \rightarrow 2H_2O_{(aq)} + O_{2(g)} + 4e^-$

$$E_{\frac{O_2}{OH^-}} = E_{\frac{O_2}{OH^-}}^{\theta} + \frac{RT}{4F}\ln\frac{[\alpha_{H_2O}][\alpha_{O_2}]}{[\alpha_{H_2}]} = 1.229\ V - 0.0591 \times pH_{Anode} = 0.401\ V\ (pH = 0)$$

Overall water splitting (HER in acid and OER in alkali): $4H^+ + 4OH^- \rightarrow 2H_2O_{(aq)} + O_{2(g)} + H_{2(g)}$

$$E_{Cell} = E_{Anode} - E_{Cathode} = 0.401\ V - 0\ V = 0.401\ V$$

To characterize the crystal structure of as-prepared binary Co-Ni hydroxide grown on carbon fiber paper (Co-Ni oxide/CFP) during an electrochemical deposition method, X-ray diffraction (XRD) patterns for electrochemically synthesized Co-Ni hydroxide/CFP with different growth time (300s and 1800s) and pure CFP substrate were obtained, as shown in **Figure S1 (a)**. In these spectra, only an obvious peak found at 2□~ 26° is belonged to (002) facet of graphite, which is originated from the CFP substrate. No distinct peaks are observed and corresponded to Co and Ni hydroxide, suggesting that as-prepared metal oxide is belonged to amorphous structure during electrochemical deposition method. To confirm the presence of

Co and Ni elements in the Co-Ni hydroxide/CFP, SEM characterization with elemental mapping was conducted, as depicted in **Figure S1(b)**. The results confirm the existence of Co and Ni on the surface of the CFP. This observation suggests that the amorphous metal hydroxide behaves like a thin film adsorbed onto the surface of the CFP substrate.

XPS analysis is performed to study the elemental composition and surface electronic states of Co-Ni hydroxide/CFP with growth time of 300s and 1800s. In the XPS spectra of Co 2p (**Figure S1 (c)**), the two main peaks are found at binding energy (BE) of 781.3 eV and 796.5 eV, separated by 15.2 eV, corresponding to the Co $2p_{3/2}$ and Co $2p_{1/2}$ spin–orbit peaks, respectively and fitted to BE of the $Co(OH)_2$ phase.[2] In the XPS spectra of Ni 2p (**Figure S1 (d)**), the two peaks are also found at 855.4 eV and 872.8 eV, separated by 17.4 eV, corresponding to the Ni $2p_{3/2}$ and Ni $2p_{1/2}$ spin–orbit peaks, respectively and fitted to BE of the $Ni(OH)_2$ phase.[3] The results showed that both Ni and Co in CoNi hydroxide/CFP with reaction time of 300s and 1800s are matched to the hydroxide phase with oxidation state of 2+.
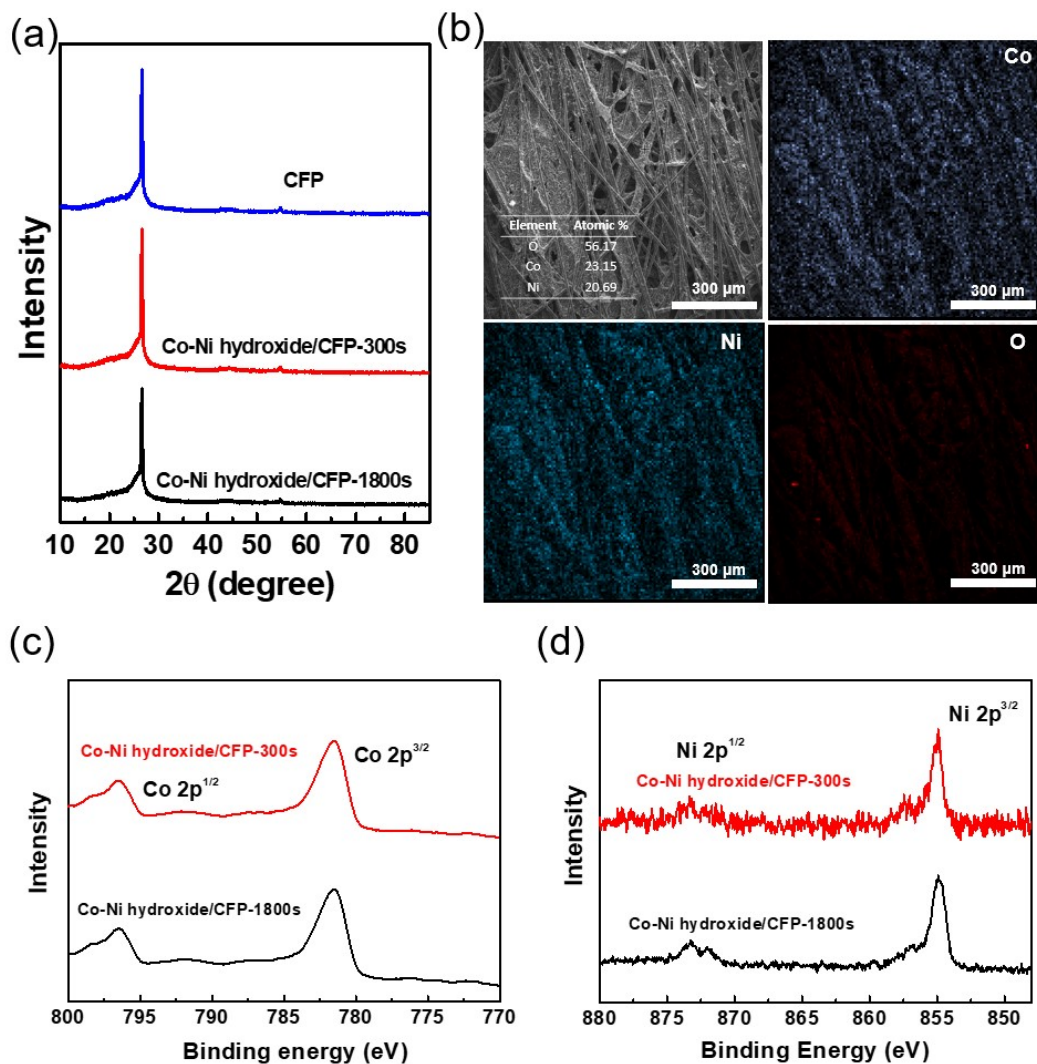
Figure S1. (a) XRD pattern of synthesized Co-Ni hydroxide/CFP with the growth time of 300s and 1800s, (b) SEM image with elemental mapping. (c) Co 2p and (d) Ni 2p of XPS spectra for representative Co-Ni hydroxide/CFP-300s.

To analyze the element distribution in the representative Co-Ni hydroxide/CFP-300s, high resolution transmission electron microscopy (HRTEM) and high-angle annular dark-field scanning transmission electron microscopy (HAADF-STEM) image were obtained along with the corresponding Energy-Dispersive X-ray Spectroscopy (EDS) element mapping of Co, Ni, O, and C elements, as shown in **Figure S2**. The HRTEM image (**Figure S2 (a)**) demonstrated the disordered atomic structure in the Co-Ni hydroxide/CFP-300s, confirming the amorphous structure, which is consistent with the image of the fast Fourier transforms (the inset in **Figure**

S2 (a)). In the HAADF-STEM image of representative Co-Ni hydroxide/CFP-300s (**Figure S2 (b)**), the brightness white color in image was belonged to Co-Ni hydroxide. From the images of EDS mapping, the signals of C, O, Co and Ni are found to be overlapped each other (merged one). According to EDS analysis, the atomic percentage of Co, Ni and O in the representative Co-Ni oxide/CFP-300s are 23.9%, 21.5% and 54.6%, respectively. Therefore, the chemical formula of Co-Ni hydroxide will be close to~ $CoNiO_{2.5}$.
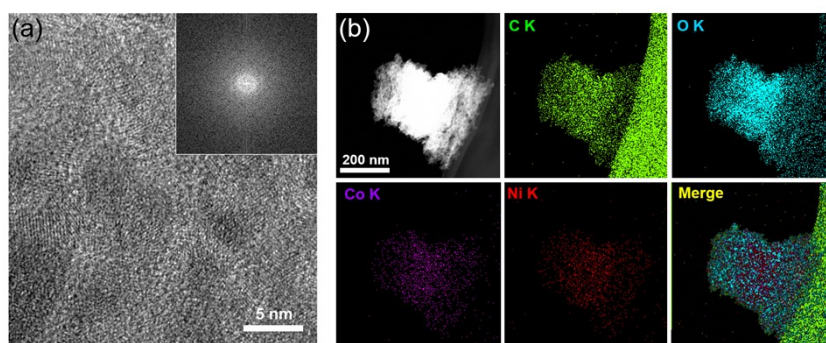

Figure S2. (a) HRTEM image of representative Co-Ni hydroxide/CFP-300s and the corresponding image of The fast Fourier transforms (inset). (b) HAADF-STEM image of representative Co-Ni hydroxide/CFP-300s and the corresponding EDS element mapping of Co, Ni, O, C elements and the merged image.

To further investigate the electronic structure and geometric structure of the amorphous Co-Ni hydroxide, the XAS analyses were employed. The XAS results of Co K-edge and Ni K-edge Co-Ni hydroxide/CFP with electrodeposition time of 300s and 1800s showed in **Figure S3**. Co K-edge and Ni K-edge X-ray near-edge fine structure (XANES) spectra reveal that both Co and Ni in Co-Ni hydroxide are in 2+ oxidation state with the edge position observed at 7713 eV (Co^{2+}) and 8338 eV (Ni^{2+}), which are matched to that of $Co(OH)_2$ and $Ni(OH)_2$, as shown in **Figure S3 (a) and (b)**, respectively. The spectra of the Co-Ni hydroxide grown for 300s and 1800s are very analogous. It presents that electronic structure and the local structure surrounding Co and Ni in these two samples are similar. To further analysis the coordination

of Co atom and Ni atom in Co-Ni hydroxide, the k^2-weighted Fourier–Transform (FT) extended X-ray absorption fine structure (EXAFS) spectra in **Figure S3 (c) and (d)**, respectively. The spectra both show that on Co-O bond and on Ni-O bond of two Co-Ni hydroxide/CFP samples located at 1.2 Å and 1.3 Å, which are similar to to that of reference $Co(OH)_2$ and $Ni(OH)_2$, respectively and no metallic Co-Co and Ni-Ni bond were found. These results illustrate that the Co and Ni atoms in the metal hydroxide materials keep randomly atomic dispersion, resulting in that the metallic Co-Co and Ni-Ni bonds don't exist in Co-Ni hydroxide.
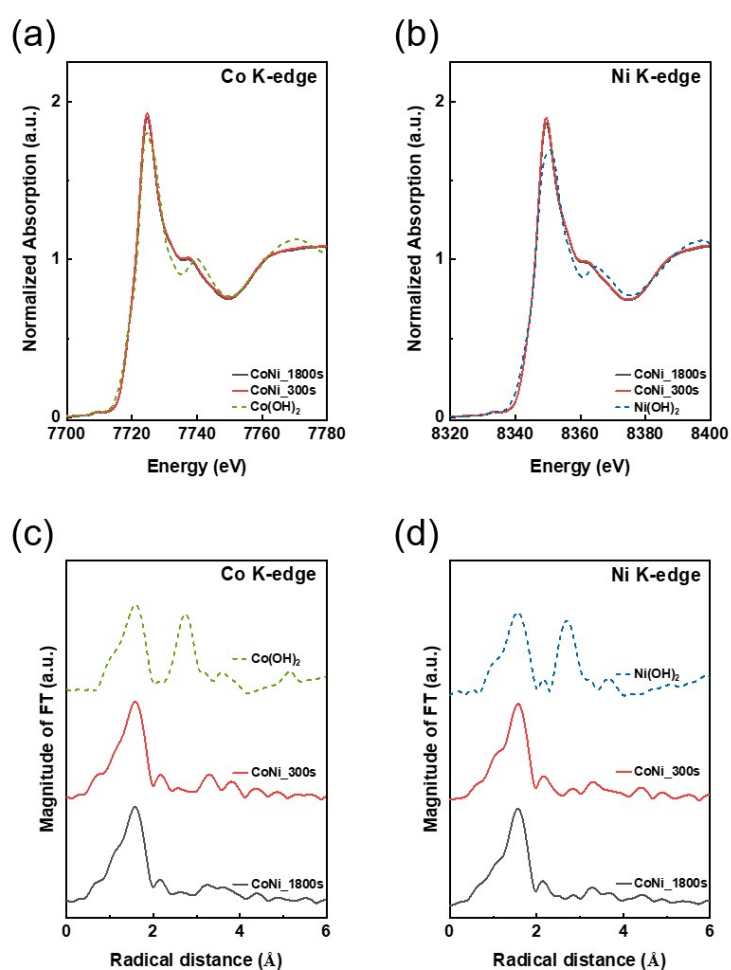

Figure S3. (a) Co K-edge and (b) Ni K-edge XANES spectra of Co-Ni hydroxide/CFP-300s and Co-Ni hydroxide/CFP-1800s. The k^2-weighted Fourier transform (c) Co K-edge and (d) Ni K-edge EXAFS spectra of Co-Ni hydroxide/CFP-300s and Co-Ni hydroxide/CFP-1800s. The reference XANES and EXAFS spectra of $Co(OH_2$ and $Ni(OH)_2$ were also provided, respectively.

To investigate the mechanism of a series of catalytic reactions on UOR process, we used the $p(2 \times 2)$ for $CoNiO_3(100)$ surface to ensure that the distance between the adsorbates are greater than an effective distance of van der Waals force. To ensure the structure of the catalyst used in the simulation was as consistent as possible with the experiment, we removed part of the oxygen atoms in the $CoNiO_3$ and further optimized it to form the most stable $CoNiO_{x\ (x=2\sim3)}$. The detailed structure for $CoNiO_{x\ (x=2\sim3)}$ (100) surface is shown in **Figure S4 (a)**. According to the experiment results, the O atoms of $CoNiO_x$ (100) are hydrogenated to form the numerous hydroxyl groups (OH). Therefore, in this work, to realistically simulate the catalytic environment $CoNiO_x(100)$, we constructed a series of $(OH_{sur})_n$-$CoNiO_x(100)$ surfaces containing different numbers of OH_{sur} in the top layer. However, as the OH concentration of the top layer on the surface of $CoNiO_x$ (100) gradually increases, we had to examine further the possibility of oxygen vacancies formed due to the generation of water. Therefore, from our calculation results, we observed that increasing the surface OH concentration will enhance the $CoNiO_x$ (100) surface stability ($\Delta G < 0$), as shown in **Figure S4 (b)**. Notably, if the surface OH concentration reaches 75%, i.e. $(OH_{sur})_8 - CoNiO_x$ (100), the subsequent increase in OH concentration will be hindered by water generation. The detail optimization structures of $(OH_{sur})_9$-$CoNiO_x(100)$ and $(OH_{sur})_7O_v$-$CoNiO_x(100)$ are represented in **Figure S4 (c)** and **Figure S4 (d)**, respectively. Based on the above calculation results, we will conduct a series of discussions on the reactivity of urea oxidation through $CoNiO_x(100)$, $(OH_{sur})_9$-$CoNiO_x(100)$ and $(OH_{sur})_7O_v$-$CoNiO_x(100)$. First, compared with the other two surfaces, we found that urea adsorbed on $(OH_{sur})_7O_v$-$CoNiO_x(100)$ has higher adsorption energy. The adsorption energies and geometric parameters for urea on these surfaces are listed in **Table S3**; the corresponding optimized structures are depicted schematically in **Figure S5**.
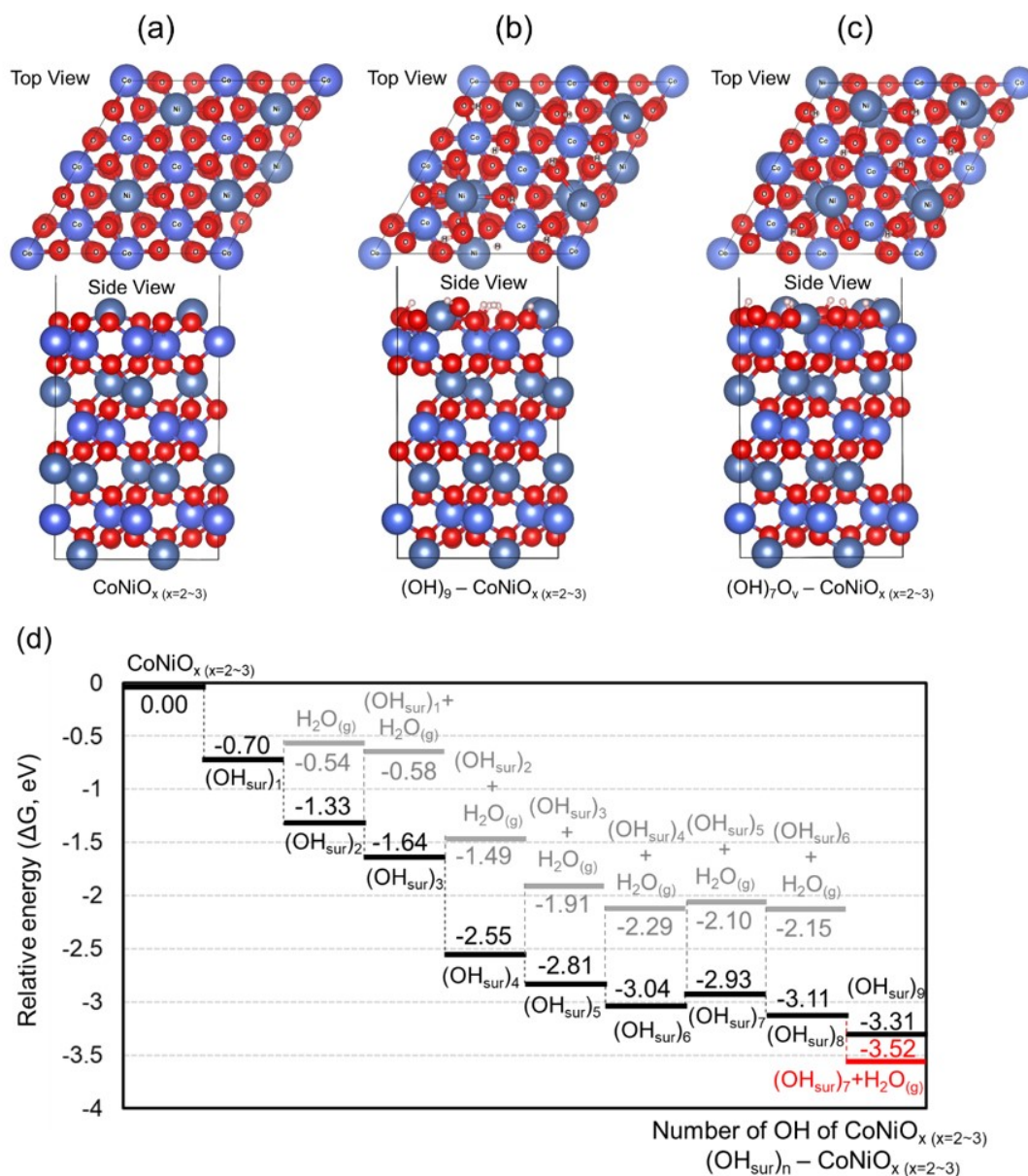
Figure S4. The schematic representations of optimized structure for (a)$CoNiO_3(100)$, (b)$(OH_{sur})_9$ - $CoNiO_{x\,(x=2\sim3)}$ (100) and (c)$(OH_{sur})_7O_v$ - $CoNiO_{x\,(x=2\sim3)}$ (100). (d)The profile of the relative energies of the different numbers of OH_{sur} in the top layer on $CoNiO_3(100)$ surface.
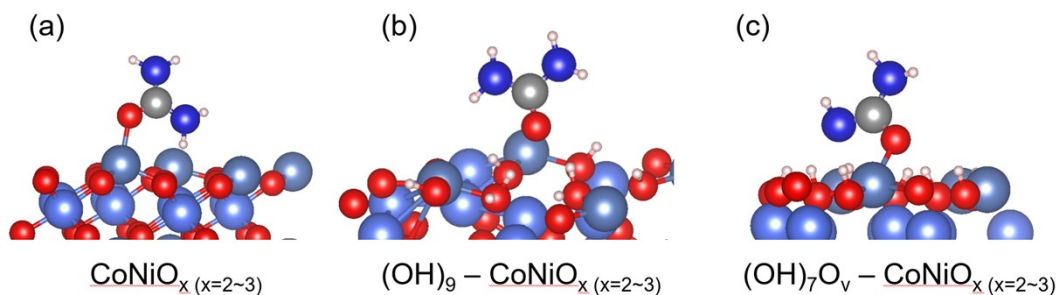
(a) $CoNiO_x$ (x=2~3) (b) $(OH)_9 - CoNiO_x$ (x=2~3) (c) $(OH)_7O_v - CoNiO_x$ (x=2~3)

Figure S5. The schematic representations of the optimized structures of the urea on (a)$CoNiO_x$ (x=2~3) (100), (b)$(OH_{sur})_9$-$CoNiO_x$ (x=2~3)(100) and (c)$(OH_{sur})_7O_v$-$CoNiO_x$ (x=2~3) (100) surfaces.
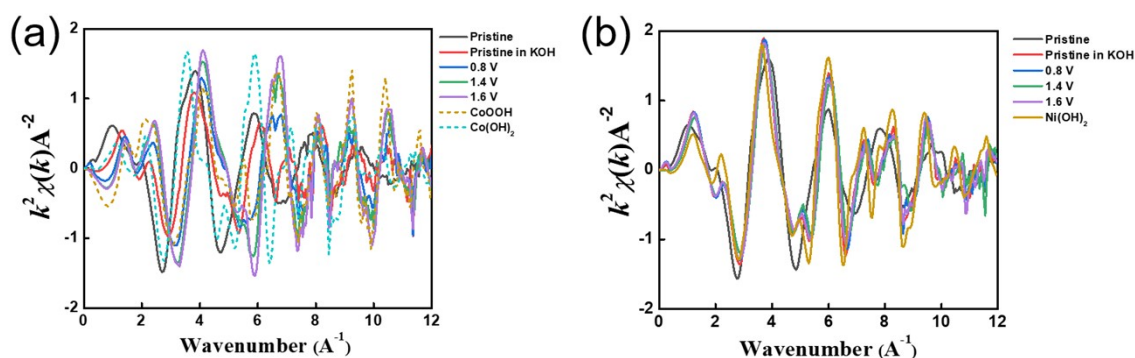

Figure S6. (a) k^2-weighted Co k-edge EXAFS of pristine Co-Ni hydroxide/CFP-300s, KOH-treated Co-Ni hydroxide/CFP-300s, Co-Ni hydroxide/CFP-300s at 0.8 V, 1.4V and 1.6V, and reference $Co(OH)_2$ and CoOOH. (c)) k^2-weighted Ni k-edge EXAFS of of pristine Co-Ni hydroxide/CFP-300s, KOH-treated Co-Ni hydroxide/CFP-300s, Co-Ni hydroxide/CFP-300s at 0.8 V, 1.4V and 1.6V, and reference $Ni(OH)_2$.

To investigate the structure stability of Co-Ni hydroxide/CFP-300s after UOR reaction, the XRD patterns and Raman spectra were obtained, as shown in **Figure S7**. The results of XRD patterns (**Figure S7 (a)**) showed the crystallinity of the Co-Ni hydroxide after UOR reaction remain ammorphous phase which is the same as the initial condition. Raman spectroscopy was used to investigate the surface chemical condition of the Co-Ni hydroxide after UOR reaction, as shown in **Figure S7 (b)**. Two strong peaks at 1352 cm^{-1} and 1575 cm^{-1} are the characteristic D band and G band of grahpite materials on carbon fiber paper,

respectively. In the pristine Co-Ni hydroxide/CFP-300s, there is no obvious signal found from 400 cm^{-1} to 600 cm^{-1}, meaning that the crystal structure of pristine sample is completely amorphous pahse. After reaction, a broad spectral feature were found in the range of 400 cm^{-1} to 600 cm^{-1}, corresponding to E_g and A_{1g} vibrational modes of Co−O in CoOOH. Although a broad spectrum was found, the crystallinily of the sample still remained low and close to amorphous CoOOH. Because the crystallinity of our Co-Ni hydroxide is quite low, Raman signals (**Figure S7 (c)**) are too weak to be collected in the electrolyte condition during UOR reaction with applying different potential. Therefore, the detailed fine structure of the Co-Ni hydroxide before and after UOR reaction were performed by using in-situ XAS during electrochemical reaction process as below.
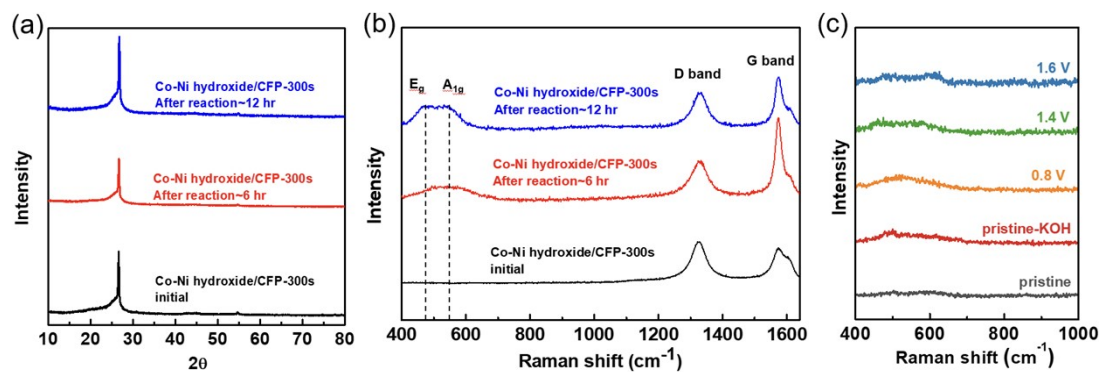

Figure S7. (a) XRD and (b) ex-situ Raman spectra of Co-Ni hydroxide/CFP before and after UOR reaction with 6 hours and 12 hours. (c) In-situ Raman spectra of Co-Ni hydroxide/CFP in the electrolyte during UOR reaction.
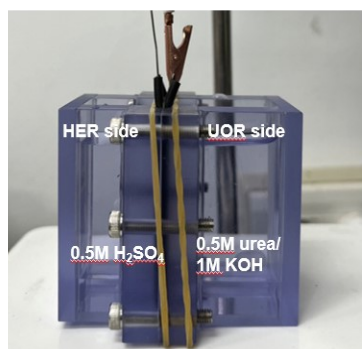
Figure S8. The image of electrochemical H-cell including two parts separated by a Nafion membrane to avoid the oxidation reaction of urea

Table S1. Comparisons of UOR performance of Blending CoOOH-Ni(OH)$_2$/CFP-300s with results in recent literatures.

Anode Catalysis	Solution	Current density	Tafel slope	Ref.
Blending CoOOH-Ni(OH)$_2$/CFP-300s	1M KOH+0.5M Urea	**1.28V /10mAcm^{-2}**	**37.2** mV dec^{-1}	(this work)
NiF$_3$/Ni$_2$P @CC	1M KOH+ 0.33M Urea	1.36V /10mAcm^{-2}	33 mV dec^{-1}	Chem. Eng. J. 2022, 427, 130865.[4]
Pt$_1$/CNT(Cl)-800	0.1 M HClO$_4$ +1 M NaCl	1.39 /10mAcm^{-2}	37 mV dec^{-1}	ACS Catalysis 2021, 11 (19), 12232.[5]
Ni@C-250	1M KOH+0.5M Urea	1.5V /100 mAcm^{-2}	43 mV dec^{-1}	Catal. Sci. Technol., 2021, 11, 2480[6]
Au@AuIr$_2$	0.5M H$_2$SO$_4$	1.53V /300 mAcm^{-2}	58.3 mV dec^{-1}	J. Am. Chem. Soc. 2021, 143, 12, 4639–4645[7]
Pt1/CNT	0.1 M HClO$_4$ +1 M NaI	1.4V /10mAcm^{-2}	38 mV dec^{-1}	Nature Commun. 2020, 11 (1), 1[8]
Ni–Co(OH)$_2$	1M KOH+ 0.33 M KI	1.36V /10mAcm^{-2}	47 mV dec^{-1}	Nanoscale Adv., 2021, 3 (2), 604.[9]
NiO/CuO @CuM	1M KOH+0.5M Urea	1.39V /100 mAcm^{-2}	32.2 mV dec^{-1}	Nano Energy, 2023. **115**.[10]
Ce-Co$_3$-O$_4$	1M KOH+0.5M Urea	1.39V /50 mAcm^{-2}	30.5 mV dec^{-1}	J Colloid Interface Sci, 2023. **630**(Pt A): p. 512-524.[11]
Zn@Ni-MOF	1M KOH+ 0.33M Urea	1.31V /10 mAcm^{-2}	-	Journal of Materials Chemistry A, 2023. **11**(27): p. 14870-14877.[12]
Ni$_x$S$_y$/NF-3	1M KOH+ 0.33M Urea	1.343V /10 mAcm^{-2}	34.8 mV dec^{-1}	Journal of Electroanalytical Chemistry, 2023. **928**.[13]

Table S2. Comparisons of a two-electrode electrolyzer for asymmetric electrocatalysis in recent literatures.

Anode Catalyst	Solution	Membrane separated	Current density	Tafel slope	Ref.
Blending CoOOH-Ni(OH)$_2$/CFP-300s	Anode: 1M KOH+0.5M Urea Cathode: 0.5M H$_2$SO$_4$	Y	0.45V /10mAcm^{-2}	37.2 mV dec^{-1}	(this work)
CFP	Anode: 0.1M HClO$_4$ +1 M NaI Cathode: 0.5M H$_2$SO$_4$	Y	0.59V /10mAcm^{-2}	47.78 mV dec^{-1}	Journal of Materials Chemistry A, 2022. **10**(45): p. 23982-23989.[14]
RuSn SAO	Anode: 0.1 M HClO$_4$ +0.1 M NaI Cathode: 0.5M H$_2$SO$_4$	Y	1.07V /10mAcm^{-2}	40 mV dec^{-1}	ACS Sustainable Chem. Eng. 2021 9 (26), 8803-8812[15]
CuCl/rGO	Anode: 1M KOH+0.5M Urea Cathode: 0.5M H$_2$SO$_4$	Y	0.83V /10mAcm^{-2}	-	Chem. Commun., 2018, 54, 2603[16]
NiCoP NW/NF	Anode: 1M KOH, Cathode: 0.5M H$_2$SO$_4$	Y	0.95V /10mAcm^{-2}	-	ACS Sustainable Chem. Eng. 2021 9 (48), 16163-16171[17]
Ru-RuO$_2$-CNT	Anode: 1.0M KOH Cathode: 0.5MH2SO4	Y	0.73V /10mAcm^{-2}	-	Nano Energy 2019, 61, 576.[18]
Co-Ni-P/NF	Anode: 1.0M NaOH Cathode: 0.5MH2SO4	Y	0.841V/ 10mAcm^{-2}	-	Carbon Energy, 2020. **2**(4): p. 646-655.[19]

Table S3. The adsorption energies (eV) and the corresponding bond lengths (Å) of urea on $CoNiO_3(100)$, $(OH_{sur})_9$-$CoNiO_3(100)$ and $(OH_{sur})_7O_v$-$CoNiO_3(100)$ surfaces.

	Urea			
Surface	E_{ads}/eV	d(C=O)/Å	d(C-N)/Å	d(M-O)/Å
$CoNiO_3(100)$	-0.61	1.26	1.34(1.36)	2.01
$(OH_{sur})_9$-$CoNiO_3(100)$	-0.36	1.25	1.36(1.37)	-
$(OH_{sur})_7O_v$-$CoNiO_3(100)$	-0.90	1.29	1.33(1.38)	1.95

Reference:

1.   Kresse, G. & Hafner, J. Ab initio molecular dynamics for liquid metals. *Physical review B* **47**, 558 (1993).

2.   Kresse, G. & Hafner, J. Ab initio molecular-dynamics simulation of the liquid-metal–amorphous-semiconductor transition in germanium. *Physical Review B* **49**, 14251 (1994).

3.   Kresse, G. & Furthmüller, J. Efficiency of ab-initio total energy calculations for metals and semiconductors using a plane-wave basis set. *Computational materials science* **6**, 15-50 (1996).

4.   Kresse, G. & Furthmüller, J. Efficient iterative schemes for ab initio total-energy calculations using a plane-wave basis set. *Physical review B* **54**, 11169 (1996).

5.   Blöchl, P.E. Projector augmented-wave method. *Physical review B* **50**, 17953 (1994).

6.   Kresse, G. & Joubert, D. From ultrasoft pseudopotentials to the projector augmented-wave method. *Physical review b* **59**, 1758 (1999).

7.   Perdew, J.P., Burke, K. & Ernzerhof, M. Generalized gradient approximation made simple. *Physical review letters* **77**, 3865 (1996).

8.   Mathew, K., Sundararaman, R., Letchworth-Weaver, K., Arias, T. & Hennig, R.G. Implicit solvation model for density-functional study of nanocrystal surfaces and reaction pathways. *The Journal of chemical physics* **140** (2014).

9. Greco, R. et al. Activation of 2D cobalt hydroxide with 0D cobalt oxide decoration for microplastics degradation and hydrogen evolution. *Chemical Engineering Journal* **471**, 144569 (2023).

10. Zhu, D. et al. A 2D metal–organic framework/Ni (OH) 2 heterostructure for an enhanced oxygen evolution reaction. *Nanoscale* **11**, 3599-3605 (2019).

11. Wang, K. et al. Engineering NiF3/Ni2P heterojunction as efficient electrocatalysts for urea oxidation and splitting. *Chemical Engineering Journal* **427**, 130865 (2022).

12. Lim, T. et al. General Efficacy of Atomically Dispersed Pt Catalysts for the Chlorine Evolution Reaction: Potential-Dependent Switching of the Kinetics and Mechanism. *ACS Catalysis* **11**, 12232-12246 (2021).

13. Wang, J. et al. Ni/NiO heterostructures encapsulated in oxygen-doped graphene as multifunctional electrocatalysts for the HER, UOR and HMF oxidation reaction. *Catalysis Science & Technology* **11**, 2480-2490 (2021).

14. Wang, H. et al. Significantly Enhanced Overall Water Splitting Performance by Partial Oxidation of Ir through Au Modification in Core-Shell Alloy Structure. *J Am Chem Soc* **143**, 4639-4645 (2021).

15. Lim, T. et al. Atomically dispersed Pt-N(4) sites as efficient and selective electrocatalysts for the chlorine evolution reaction. *Nat Commun* **11**, 412 (2020).

16. Hu, E. et al. Boosting hydrogen generation by anodic oxidation of iodide over Ni-Co(OH)(2) nanosheet arrays. *Nanoscale Adv* **3**, 604-610 (2021).

17. Yang, L. et al. Self-supported NiO/CuO electrodes to boost urea oxidation in direct urea fuel cells. *Nano Energy* **115**, 108714 (2023).

18. Wang, H., Du, X., Zhang, X. & Li, L. Controlled synthesis of M doped Co(3)O(4) (M = Ce, Ni and Fe) on Ni foam as robust electrocatalyst for oxygen evolution reaction and urea oxidation reaction. *J Colloid Interface Sci* **630**, 512-524 (2023).

19. Shrestha, N.K., Patil, S.A., Salunke, A.S., Inamdar, A.I. & Im, H. Unprecedented urea oxidation on Zn@Ni-MOF with an ultra-high current density: understanding the competition between UOR and OER, catalytic activity limitation and reaction selectivity. *Journal of Materials Chemistry A* **11**, 14870-14877 (2023).

20. Liu, H., Wen, D. & Zhu, B. In-situ growth of hierarchical nickel sulfide composites on nickel foam for enhanced urea oxidation reaction and urine electrolysis. *Journal of Electroanalytical Chemistry* **928**, 117082 (2023).

21. Peng, S.-M. et al. Fast charge transfer between iodide ions and a delocalized electron system on the graphite surface for boosting hydrogen production. *Journal of Materials Chemistry A* **10**, 23982-23989 (2022).

22. Adam, D.B. et al. Iodide Oxidation Reaction Catalyzed by Ruthenium–Tin Surface Alloy Oxide for Efficient Production of Hydrogen and Iodine Simultaneously. *ACS Sustainable Chemistry & Engineering* **9**, 8803-8812 (2021).

23. Wang, G. et al. Energy-efficient electrolytic hydrogen production assisted by coupling urea oxidation with a pH-gradient concentration cell. *Chem Commun* **54**, 2603-2606 (2018).

24. Wei, Z. et al. Asymmetric Electrolyte Design: Energy-Efficient Electrolytic Hydrogen Production under 0.95 V Driven by Janus Metal Phosphide Nanoarray. *ACS Sustainable Chemistry & Engineering* **9**, 16163-16171 (2021).

25. Zhang, M. et al. Ru-RuO2/CNT hybrids as high-activity pH-universal electrocatalysts for water splitting within 0.73 V in an asymmetric-electrolyte electrolyzer. *Nano Energy* **61**, 576-583 (2019).

26. Xu, J. et al. Stable overall water splitting in an asymmetric acid/alkaline electrolyzer comprising a bipolar membrane sandwiched by bifunctional cobalt-nickel phosphide nanowire electrodes. *Carbon Energy* **2**, 646-655 (2020).